ELSEVIER

Contents lists available at ScienceDirect

# International Journal of Multiphase Flow

journal homepage: www.elsevier.com/locate/ijmulflow





# Investigating atomization characteristics in an electrostatic rotary bell atomizer

Venkata Krisshna\*, Mark Owkes

Montana State University, Department of Mechanical & Industrial Engineering, P.O. Box 173800, Bozeman, MT 59717-3800, USA

#### ARTICLE INFO

#### Keywords: NGA Electrohydrodynamics Multiphase flow Atomization Droplet genealogy

#### ABSTRACT

Electrostatic rotary bell atomizers are commonly used in several engineering applications, including the automobile industry. A high-speed rotating nozzle operating in a strong background electric field atomizes paint into charged droplets that range from a few micrometers to tens of micrometers in diameter. The atomization process directly determines the droplet size and droplet charge distributions which subsequently control the transfer efficiency and the surface finish quality. We have previously developed a tool to perform high fidelity simulations of near-bell atomization with electrohydrodynamic effects. In this work, we perform simulations employed with a droplet ancestry extraction tool to analyze previously inaccessible information and understand the physical processes driving atomization. We find that the electric field accelerates breakup processes and enhances secondary atomization. The total number of droplets, the ratio of secondary to primary droplets, and the ratio of coalescence to breakup activity are all much higher when operating in an electric field. We analyze the droplet velocity, local Weber number and charge density statistics to understand the complex physics in electrically assisted breakup. The results of the study have helped us gain insights into the physics of atomization in electrostatic rotary sprays.

# 1. Introduction

Electrostatic rotary bell atomizers (ERBAs) (Fig. 1) are commonly used as automotive painting devices. In addition to automobile paint shops, rotary atomizers are used in several other applications such as agricultural spraying (Craig et al., 2014), food processing (Oxley, 2012), and pharmaceutical drug-delivery (Mackaplow et al., 2006). In an ERBA, a high speed rotating nozzle operating in a strong background electric field atomizes paint into a spray of charged droplets. Paint is charged and injected into a bell-shaped nozzle where it forms a thin film due to centrifugal forces. The fluid film exits the edge of the nozzle to form ligaments which further atomize into droplets (Frost, 1981). Electrification of the device is carried out to improve its transfer efficiency (TE) (Domnick and Thieme, 2006; Im et al., 2000). The charged droplets move through the background electric field towards the grounded target surface.

Electrified flows are described by electrohydrodynamics (EHD)—the science of characterizing interactions between fluid dynamics and electrostatics (Chen et al., 2003; Fylladitakis et al., 2014). EHD has seen several decades of research and is now employed in various engineering applications including food technology (Anukiruthika et al., 2021; Khan et al., 2012; Gorty and Barringer, 2011), inkjet printing (Raje and Murmu, 2014), electrostatic precipitation (Yamamoto

and Velkoff, 1981), powder coating (Jaworek et al., 2018), biochemistry (Stimpson and Evans, 1978), microfluidics (Azizian et al., 2019), fuel injection (Fredrich et al., 2022; Shrimpton and Laoonual, 2006), and biomedical applications (Enayati et al., 2011; Eagles et al., 2006; Farook et al., 2007). EHD-assisted liquid atomization, a process first highlighted by the works of Kim and Turnbull (1976) and Kelly (1984) has been an increasingly important means of producing liquid droplets that is well-established to offer advantages over other industrial spraying processes (Bailey, 1974; Hayati et al., 1986; Grace and Marijnissen, 1994).

The optimal performance of ERBAs can be improved, for example, in the automotive painting industry. Currently, painting with ERBAs often requires over-coating to ensure sufficient finish quality (Sadegh et al., 2018). This has an effective reduction in its overall TE. The operation of ERBAs can be improved to prevent using excess paint to achieve sufficient surface finish quality (Sadegh et al., 2018). The process of painting vehicles is one of the most expensive aspects of automobile manufacturing, accounting for up to 50% of its total costs (Akafuah et al., 2013; Clément et al., 2014). With the global automotive paints and coatings market size expected to value about \$26.8 bn by 2027 (Precedence Research, 2019), small improvements can result in significant cost savings and waste reduction. Additionally, the

E-mail addresses: venkat.krisshna@student.montana.edu (V. Krisshna), mark.owkes@montana.edu (M. Owkes).

<sup>\*</sup> Corresponding author.



Fig. 1. A rotary bell atomizer in operation.

Source: Photograph courtesy of RISE Research Institutes of Sweden and Fraunhofer-Chalmers Centre.

paint shop is responsible for over 80% of the environmental concerns in an automobile manufacturing facility (Geffen and Rothenberg, 2000). Advancing our understanding of the breakup mechanisms of ERBAs can improve the financial and environmental impact of the device in the automotive, agricultural, and pharmaceutical industries.

Crucial metrics such as the droplet size uniformity, surface finish quality, TE, deposition thickness, and environmental impact are directly dependent on the atomization process of ERBAs (Domnick and Thieme, 2006; Akafuah et al., 2016; Corbeels et al., 1992). Currently, expensive trial-and-error experimentation is used to find optimal operating conditions in industrial applications of ERBAs.

Rotary atomization of uncharged sprays has been well studied by several groups experimentally (Hinze and Milborn, 1950; Balachandran and Bailey, 1984; Domnick, 2010; Mahmoud and Youssef, 2014; Naoki et al., 2019; Corbeels et al., 1992; Loch et al., 1998; Dombrowski and Lloyd, 1974; Shen et al., 2019; Ogasawara et al., 2010; Keshavarz et al., 2020; Ahmad et al., 2019; Rezayat and Farshchi, 2019; Sidawi et al., 2021a,b; Stevenin et al., 2015). Although imaging equipment are seldom placed in ERBA setups to prevent electric arcing (Gödeke et al., 2021), recent efforts using ballistic (Linne et al., 2005; Sedarsky et al., 2010; Slangen et al., 2016) and X-ray (Wang et al., 2006; Heindel, 2018; Li et al., 2021) technologies are able to provide snapshots of the atomization and spray transfer processes (Darwish Ahmad et al., 2018; Wilson et al., 2018; Ahmad et al., 2019; Hines, 1966; Im et al., 2000; Im\* et al., 2003; Im et al., 2004). The articles listed above, however, lack the analysis of the temporal information of the flow, which can help investigate breakup mechanisms. Tracking algorithms for experimental studies that rely on image processing techniques have been developed in the past to identify breakup and coalescence activity in bubble and droplet flows (Rodríguez-Rodríguez et al., 2003; Rodriguez-Rodriguez et al., 2006; Honkanen et al., 2011). However, it is still extremely challenging to analyze droplet breakup dynamics using visual snapshots because of the length and time scales of the process. Moreover, the process of charge transport dynamics are inaccessible to visual analysis (Wilson et al., 2018).

Recent numerical efforts have characterized the effects of various operating parameters on droplet trajectories, droplet size distribution, spray pattern, and charge evaporation in ERBAs (Viti et al., 2010; Domnick et al., 2005, 2006; Colbert and Cairncross, 2005; Colbert, 2007; Ellwood et al., 2014; Pendar and Páscoa, 2019, 2020; Ray and Henshaw, 2018; Guettler et al., 2020; Mark et al., 2013; Krisshna and Owkes, 2023). High-fidelity numerical simulations, which can resolve the relevant time and length scales, can be used to extract droplet ancestry statistics as a valuable means of understanding the physics

of atomization in complex systems (Saye et al., 2023). In this work, a droplet ancestry extraction tool first introduced by Rubel and Owkes (2019) and further developed by Christensen and Owkes (2023) is employed to extract and store droplet and local flow field statistics during each breakup and coalescence event in simulations of near-bell atomization in ERBAs. The information is stored in a Neo4j graphical database and analyzed to track the evolution of the liquid as it moves from the liquid core to small droplets in an atomizing flow. The analysis allows us to compute breakup and coalescence statistics, which characterize the drop size distributions and help understand the physics of atomization using high-fidelity simulations.

Using the droplet ancestry extraction tool, we conduct numerical experiments to investigate the droplet conditions and local flow field characteristics to understand the underlying mechanisms influencing electrically-assisted rotary atomization. The findings of this work can provide insight towards optimizing ERBAs for operational cost and environmental impact.

The article is organized as follows — the governing equations used to describe the numerical model of atomization in ERBAs are detailed in Section 2. The simulation setup including the ancestry extraction tool is discussed in Section 3. Inferences from a comparative study to examine the effect of electrification on atomization are presented in Section 4. Section 5 contains the summary of this project and potential future work that can be conducted to study atomization in ERBAs.

#### 2. Governing equations

The physics modules discussed below have been implemented within a code called NGA — a high-order, fully conservative, variable density, low Mach number Navier–Stokes solver that contains various multi-physics modules implemented in parallel using message passing interface (MPI). The formulation discretely conserves mass and momentum in a periodic domain. NGA uses a conservative unsplit geometric volume-of-fluid (VOF) scheme as described in the works of Blanquart et al. (2009), Desjardins et al. (2008a,b) and Owkes and Desjardins (2014, 2015a,b, 2017). NGA has been developed by several groups to solve multiphase EHD flows, details of which can be found in Van Poppel et al. (2010), Sheehy and Owkes (2017), and Krisshna and Owkes (2023).

#### 2.1. Multiphase fluid dynamics

For low-Mach number, variable density, multiphase flows, mass and momentum conservation laws in both phases can be written as follows

$$\frac{\partial \rho_i}{\partial t} + \nabla \cdot (\rho_i \mathbf{u}_i) = 0 \tag{1}$$

$$\frac{\partial \rho_{i} \mathbf{u}_{i}}{\partial t} + \nabla \cdot (\rho_{i} \mathbf{u}_{i} \otimes \mathbf{u}_{i}) = -\nabla p_{i} + \nabla \cdot (\sigma_{i}^{f} + \sigma_{i}^{e}) + \gamma \kappa \mathbf{n} \delta_{s} + \mathbf{f}_{\text{external}}$$
(2)

where  $\rho$  is the density,  $\mathbf{u}$  is the velocity field vector, t is time, and p is the hydrodynamic pressure. The subscript t denotes the fluid phase (gas or liquid). The term  $\gamma \kappa \mathbf{n} \delta_s$  denotes surface tension force, where  $\gamma$  is the surface tension coefficient,  $\kappa$  is the local curvature of the interface computed using the ACES technique (Owkes et al., 2018),  $\mathbf{n}$  is the normal vector to the interface, and  $\delta_s$  is a Dirac-delta function that is nonzero only on the interface (Owkes and Desjardins, 2015b). The viscous stress tensor  $\sigma_s^t$  in Eq. (2) is given by

$$\boldsymbol{\sigma}_{i}^{\mathrm{f}} = \mu_{i}(\nabla \mathbf{u}_{i} + \nabla \mathbf{u}_{i}^{\mathrm{T}}) - \frac{2}{3}\mu_{i}(\nabla \cdot \mathbf{u}_{i})\mathbb{I}$$
(3)

where  $\mu$  is the dynamic viscosity and  $\mathbb{I}$  is the identity tensor.

These equations form the basis of the fluid dynamics module in this work and further details can be found in Owkes and Desjardins (2017, 2014) and Desjardins et al. (2008a,b).  $\sigma_i^e$  is the Maxwell stress tensor which will be described later in this section.  $\mathbf{f}_{\text{external}}$  is a combination of the forces experienced by a fluid element in the system.

$$\mathbf{f}_{\text{external}} = \mathbf{f}_{\text{centrifugal}} + \mathbf{f}_{\text{Coriolis}} + \mathbf{f}_{\text{gravity}} \tag{4}$$

#### 2.2. Electrohydrodynamics

The Maxwell stress tensor  $\sigma_i^e$  in Eq. (2) is given by

$$\sigma_i^{\text{e}} = \varepsilon_i \mathbf{E}_i \otimes \mathbf{E}_i - \frac{\varepsilon_i}{2} \mathbf{E}_i \cdot \mathbf{E}_i \left( 1 - \frac{\rho_i}{\varepsilon_i} \frac{\partial \varepsilon_i}{\partial \rho_i} \right) \mathbb{I}$$
 (5)

where E is the electric field vector and  $\varepsilon$  is the electric permittivity equal to the product of the relative permittivity  $\kappa_i$  and the vacuum permittivity space  $\varepsilon_0$ . Magnetic effects have been ignored since the EHD time scale is several orders of magnitude larger than the magnetic time scale (Saville, 1997) in the atomization process that is of interest here. This electrostatic assumption eliminates the effect of the velocity of the charges (i.e., current) on the electric field thus dictating that the electric field is only influenced by the instantaneous electric charge distribution. The electric force can be expressed as the divergence of the Maxwell stress tensor,

$$\nabla \cdot \boldsymbol{\sigma}_{i}^{e} = q_{i} \mathbf{E}_{i} - \frac{1}{2} \mathbf{E}_{i}^{2} \nabla \boldsymbol{\varepsilon}_{i} + \nabla \left( \frac{1}{2} \rho_{i} \frac{\partial \boldsymbol{\varepsilon}_{i}}{\partial \rho_{i}} \mathbf{E}_{i}^{2} \right)$$
 (6)

where q is the volumetric electric charge density. The first term on the right-hand side of Eq. (6) is the Coulomb (or Lorentz) force. The second and third terms denote the dielectric and the electrostrictive forces respectively, which are only significant in a transient electric field with time scales several orders of magnitude larger than what is encountered in atomization problems (Kourmatzis and Shrimpton, 2009).

As the electric field vector is irrotational it can be expressed in terms of the scalar electric potential  $\phi$  as

$$\mathbf{E}_{i} = -\nabla \phi. \tag{7}$$

The electric potential Poisson equation describes the relationship between charge density  $q_i$  and  $\phi$  as

$$-\nabla \cdot (\varepsilon_i \nabla \phi) = q_i. \tag{8}$$

The accumulation of bulk volumetric charge as a surface charge in a thin electric boundary layer much smaller than the hydrodynamic boundary layer is a commonly made assumption in charged jet simulations (Wang et al., 2019; Turnbull, 1989). The electric charge has previously been modeled in two ways: either a constant bulk volumetric charge or a fully relaxed surface charge. According to the classic leaky dielectric model (Melcher and Taylor, 1969; Taylor, 1966; Saville, 1997) that is commonly used to describe the effects of electric charge in dielectric liquids, the fundamental underlying assumption is that bulk volumetric electric charge has sufficient time to fully relax to a surface charge. However, for atomizing flows the advection time scale is similar to the charge relaxation time scale and a fully relaxed charge assumption is invalid. The charge relaxation time  $\tau_q$  represents the time required for volumetric charge  $q_l$  to relax to the surface (Crowley, 1986; Kourmatzis and Shrimpton, 2009). The fluid advection timescale  $\tau_f$  is a characteristic time for a fluid element to move across a relevant length scale  $L_0$ . The ratio of the two time scales called the electric Reynolds number Re<sub>e</sub> was formulated in Stuetzer (1962) as

$$\tau_q = \frac{\varepsilon_l}{\psi_l \, q_l},\tag{9}$$

$$\tau_f = \frac{L_0}{\mathbf{u}}, \tag{10}$$

$$\operatorname{Re}_e = \frac{\tau_q}{\tau_f} \tag{11}$$

$$Re_e = \frac{\tau_q}{\tau_c} \tag{11}$$

where values of the quantities that correspond to typical automotive paints and ERBA operations listed in Table 1 yield a value of Re, approximately equal to 8.93. This suggests that the advection and charge relaxation timescales are comparable in this application. The above time scale analysis highlights the necessity to model the process of charge relaxation by migration and diffusion in addition to advection with the fluid velocity. The common assumption of charges to be accumulated on the surface disallows the charge migration dynamics and limits the accuracy of the droplet charge distribution after atomization. In this work, we assume a constant bulk volumetric charge at the injector and allow charges to relax as the jet propagates through the domain. Charge transport is described by the conservation equation

$$\frac{\partial q_i}{\partial t} + \nabla \cdot \mathbf{J}_i = 0 \tag{12}$$

where the current density J<sub>i</sub> is formulated as (Melcher, 1981; Van Poppel et al., 2010)

$$\mathbf{J}_{i} = q_{i}\mathbf{u}_{i} + q_{i}\psi_{i}\mathbf{E}_{i} - \mathcal{D}_{i}\nabla q_{i} \tag{13}$$

where  $\psi_i$  is the charge mobility coefficient and  $\mathcal{D}_i$  is the molecular diffusivity. The three terms that contribute to the current density can be described as advection due to the velocity field, advection due to the electrical velocity, and diffusion.

In summary, the charge density field (q) and boundary conditions (BCs) in electric potential are used to obtain the electric potential field  $(\phi)$  using Eq. (8). The electric field (E) is then obtained using Eq. (7) after which Eq. (6) allows for the calculation of the electric (Coulomb) force on the charged fluid. More details on the validation and the demonstration of the EHD module can be found in Sheehy and Owkes (2017) and Krisshna and Owkes (2023) respectively.

#### 2.3. Rotating reference frame

In an ERBA undergoing ligament breakup mode, while ligaments exiting the serrated bell are similar, they can vary slightly in their diameters and velocities due to variations in the film thickness leading up to the grooves. However, for simplicity, we make the assumption that individual ligaments are statistically similar to yield identical droplet size distribution and charge transport behavior. This allows us to focus on one ligament ejected from the bell edge in our numerical simulations. We attach our reference frame to the rotating nozzle and ligament.

To account for the rotating nozzle and the consequent forces, we include equations that describe the rotating reference frame. This subjects the liquid to centrifugal and Coriolis forces which can be formulated as

$$\mathbf{f}_{\text{centrifugal}} = -\rho_i \boldsymbol{\omega} \times (\boldsymbol{\omega} \times \mathbf{r}) \tag{14}$$

$$\mathbf{f}_{\text{Coriolis}} = -2\rho_i \boldsymbol{\omega} \times \mathbf{u}_i \tag{15}$$

where  $\omega$  is the angular velocity and  $\mathbf{r}$  is the radial distance from the axis of rotation. A validation of the rotating frame module is presented in Krisshna and Owkes (2023).

#### 2.4. Non-Newtonian viscosity relationship

Most modern automotive paints are non-Newtonian, particularly shear-thinning, in behavior. In this work, the viscosity of a liquid  $(\mu_l)$ subject to a local shear rate  $(\eta)$  is formulated using a modified power law as

$$\mu_l = Y_1 \cdot \eta^{(Y_2 - 1)} + Y_0 \tag{16}$$

where  $Y_0$ ,  $Y_1$ , and  $Y_2$  are viscosity coefficients (Table 1) obtained by applying a fitting function to empirical viscosity-shear rate data corresponding to automotive paints provided by PPG Industries (Fig. 2). It is notable that the viscosity of the automotive paint modeled in this work asymptotes to a value at an infinite shear rates.

# 3. Setup of numerical simulations

#### 3.1. Domain setup

The numerical setup follows the framework described in Krisshna and Owkes (2023). The domain (Fig. 3) has dimensions of 12.96 mm  $\times$  960  $\mu m \times 360~\mu m$  with a cell resolution of 3240  $\times$  240  $\times$  90 to yield 15 cells across the jet diameter.

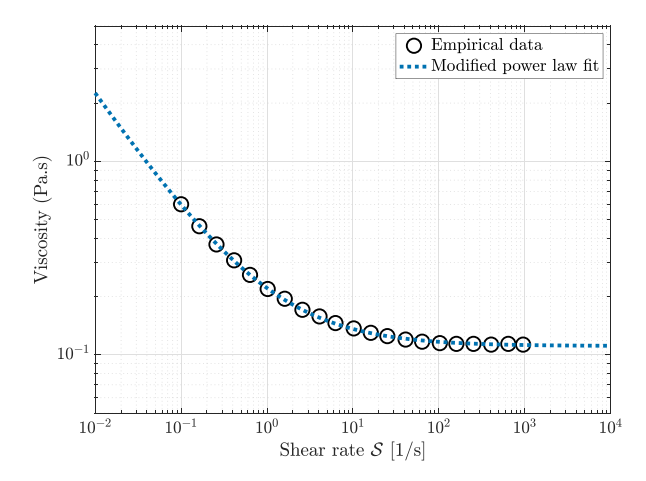


Fig. 2. The viscosity-shear rate relationship of automotive paint is approximated well using a modified power law fit (dotted line). Empirical properties of the viscous behavior of automotive paints (circles) was provided by PPG Industries. Note the logarithmic scale on the axes.

In this work, a bell of radius 25 mm is simulated. Some ERBAs are equipped with serrations present at the edge of the bell which causes the fluid to be ejected as thin jets. The bell simulated in this work is equipped with 418 serrations along its edge. We approximate a single 60 µm diameter jet that exits the bell edge when operating at 40 kRPM (Domnick et al., 2005). A magnitude of 2.879 C/m<sup>3</sup> for liquid charging is commonly applied to the dielectric liquid in industrial paint shops (Ellwood and Braslaw, 1998; Pendar and Páscoa, 2021). Charging of the liquid is done in one of many ways — by applying a voltage to the rotating bell (direct charging) (Domnick et al., 2005) or by imparting a charge to the droplets through the interaction with free ions produced by a corona discharge (external charging) (Domnick et al., 2006). However, the charging of the liquid is not the focus of this work. While the charging mode in practice does not typically yield a uniform bulk initial charge distribution, we assume such a case for simplicity. It is worth noting that the charges are still free to redistribute via advection, diffusion, and migration once the fluid leaves the bell, i.e., enters the computational domain. In future work, more complex initial charge distributions will be simulated to account for a non-uniform distribution of charge in the liquid.

The left boundary is a no-flux wall and the top boundary is a wall that permits slip velocity. The bottom and right boundaries are modeled to behave as convective outflows. Periodic BCs are imposed for mass, momentum, charge, and electric field on the front and back walls. This means that at any instance the single jet simulated in the computational domain is solved with full consideration of its nearest neighboring jets.

It is challenging to obtain accurate electric potential  $(\phi)$  boundary conditions (BCs) on the boundaries of the computational domain. Well defined  $\phi$  exists at the bell which is maintained at a high potential, and at the target surface which is grounded. For this reason, a second domain called e-Mesh that spans from the bell to the target surface is initialized and used exclusively to obtain accurate BCs of  $\phi$  on the flow domain. e-Mesh is equipped with well defined  $\phi$  boundary conditions and the charge density field, which is transferred from the flow domain. Using these, the electric Poisson equation (Eq. (8)) is solved in e-Mesh to obtain a potential field  $\phi$ . Values of  $\phi$  are transferred from e-Mesh to the boundaries of the flow domain which serve as BCs to compute  $\phi$  in the flow domain. More details on the numerical setup can be found in Krisshna and Owkes (2023).

The electric potential field (Fig. 4) in the domain ranges from the bell potential (80 kV) to about 20 kV in the absence of a liquid phase. The presence of liquid affects the  $\phi$  and E fields. The fields change depending on the location of the spray and can cause droplets to repel each other. In the figure, the trajectory of a liquid jet is graphically

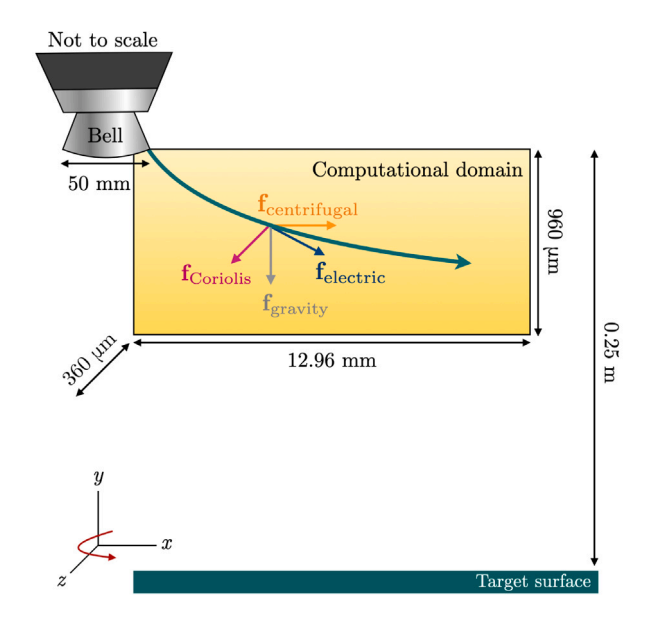


**Fig. 3.** A schematic representation of the domain geometry showing the trajectory of the liquid jet (green arrow) and the external body forces acting upon it (not to scale). (For interpretation of the references to color in this figure legend, the reader is referred to the web version of this article.)

Table 1
Standard values of parameters in the ERBA simulations.

Property	Symbol	Value	Unit
Bell rotation rate	ω	$40 \times 10^{3}$	RPM
Bell radius	$R_{bell}$	0.025	m
Edge angle		25	degrees
Inlet jet diameter	$D_{iet}$	$60 \times 10^{-6}$	m
Liq. flow rate		$7.957 \times 10^{-9}$	$m^3/s$
Gas viscosity	$\mu_{g}$	$1.8 \times 10^{-5}$	Pa.s
Liq. density	$\rho_{l}$	1000	kg/m <sup>3</sup>
Gas density	$\rho_{g}$	1.204	kg/m <sup>3</sup>
Surface tension	γ	0.03	N/m
Bell electric potential	$V_{\mathrm{bell}}$	$80 \times 10^{3}$	V
Liq. charge density	$q_l$	2.879	C/m <sup>3</sup>
Liq. rel. permittivity	$\kappa_{l}$	50	_
Gas rel. permittivity	$\kappa_{g}$	1	_
Liq. molecular diffusivity	$\mathring{\mathcal{D}_{I}}$	$2 \times 10^{-6}$	$m^2/s$
Liq. ionic mobility	$\psi_l$	$1.79 \times 10^{-8}$	$m^2/V$ s
	$Y_0$	0.11	Pa s
Liq. viscosity coefficients	$Y_1$	0.11	Pa s
	$Y_2$	0.36	-

shown as a dashed white line for reference. The contour lines of electric potential, shown as solid lines, are almost parallel to the *y*-axis in this regime. This indicates that the electric field and the electric force vectors are oriented perpendicular to the *y*-axis, i.e., in the direction of lower potential. Even in the presence of liquid in the domain, the force vector acts along the +*x*-direction in the liquid phase. A schematic representation of the direction of the electric force (blue line) acting on a control volume (blue circle) is shown for clarity. It is important to note that the electric force acts along the radially outward direction of the liquid jet in this regime as this has significant effects on the flow development which will be discussed in the following sections.

#### 3.2. Droplet ancestry extraction tool

A droplet ancestry extraction algorithm, developed and demonstrated on atomizing flows by Rubel and Owkes (2019) and Christensen and Owkes (2023), is incorporated into the ERBA simulation tool demonstrated in Krisshna and Owkes (2023) to track, collect, and store statistics of droplet breakup and coalescence events throughout

**Fig. 4.** The electric potential field and its corresponding contour lines on an x-y plane in a domain devoid of any liquid phase. The trajectory of the liquid jet is shown graphically as a dashed white line for reference. The electric force vector (blue arrow) that acts on a control volume (blue circle) in this regime is also schematically represented. The presence of liquid will affect the  $\phi$  and E fields but preserve the direction of the electric force vector. The bell is shown at the top left corner and is not to scale. (For interpretation of the references to color in this figure legend, the reader is referred to the web version of this article.)

 Table 2

 Non-dimensional numbers used in the ERBA simulations.

Number	Definition	Value
Density ratio	$\rho_l/\rho_g$	830.56
CFL	$ \mathbf{u}_{\max} \Delta t/\Delta x$	0.30
Bulk Weber	$\rho_l  \mathbf{u}_{\rm iet} ^2 \mathrm{D}_{\rm iet} / \gamma$	77.87
Permittivity ratio	$\kappa_l/\kappa_g$	50.00
Electric Reynolds (Re <sub>e</sub> )	$\epsilon_l  \mathbf{u}_{\text{iet}} /(Lq_l\psi_l)$	8.93
Electric Péclet (Pe,)	$q_l \psi_l L^2 / (\mathcal{D}_l \varepsilon_l)$	0.21
Electric Bond	$\epsilon_l  E ^2 L/\gamma$	0.091
Electro-inertial	$q_l^2 L^2 / \left( \epsilon_l \rho_l  \mathbf{u}_{\text{jet}} ^2 \right)$	0.0017

the simulation. The droplet ancestry algorithm identifies breakup and coalescence events at every time-step. Important statistics including the location, volume, local flow field, shape, and electric charge are stored for each breakup and coalescence event.

The algorithm operates through the implementation of two identification numbers, namely the structure ( $\mathcal{S}$ ) and liquid ( $\mathcal{L}$ ) identification numbers.  $\mathcal{S}$  is a unique integer computed for each liquid structure using a connected component labeling algorithm (Hoshen and Kopelman, 1976; Hendrickson et al., 2020).  $\mathcal{L}$  is a unique integer that moves with the liquid providing a time history of the fluid. Once the breakup and coalescence events have been identified using  $\mathcal{S}$  and  $\mathcal{L}$ , details on each event are extracted including the droplet size and shape, flow condition, and charge density of parent and child droplets. An exhaustive description of the underlying algorithm governing the data extraction is provided in the cited works.

#### 4. Results and discussion

Two simulations are performed – one in a non-electrified setup and one in an electrified setup – in a domain as described in Section 3.1 with parameter values listed in Table 1. The two simulations are identical except that there is no background electric potential and no liquid charge density in the former. The two cases are simulated to help understand the effect of charges and the background electric field on the breakup mechanisms driving atomization. The results section is organized as follows — We briefly present a non-dimensional analysis of the simulation parameters and discuss the relevant physical processes in this setup. We then visually compare the liquid interfaces of the two simulated cases and also show a graphical interpretation of droplet ancestry. Finally, we quantify the differences between the two simulated cases and draw inferences by discussing the overall spray characteristics and droplet statistics including size, shape, velocity, and charge density. Apart from transient results, statistics are computed after the jet has reached a quasi-steady condition, i.e., the trends in the results are maintained through time.

# 4.1. Examining non-dimensional quantities

The non-dimensional numbers corresponding to the simulations are listed in Table 2. In the interest of understanding the effect of EHD on the flow, we present a brief discussion on the relevant non-dimensional

numbers. The electric Reynolds number (Re, ) (Stuetzer, 1962) is the ratio of the charge advection timescale to the charge mobility timescale while the electric Péclet number (Pe,) (Sheehy and Owkes, 2017) is a measure of the charge mobility timescale to the charge diffusion timescale. For high values of Re, charge migration is insignificant and the initial charge distribution will prevail in the liquid jet. For low values of Re, charge migration acts quickly to relax the charges to the surface allowing for surface charge models to be appropriate. For high values of Pe, charge migration dominates the charge diffusion process and vice versa. Based on the values of Re, and Pe, for this setup, it is reasonable to model all three charge dynamics processes, i.e., advection, diffusion, and migration, since their timescales are comparable to one another. The electric Bond number (Berthier and Brakke, 2012) quantifies the importance of the deforming electrical force compared to the restoring surface tension force. A low value signifies the dominance of surface tension-driven breakup activity. The electro-inertial number (Sheehy and Owkes, 2017) denotes the importance of EHD forces compared to inertial advective forces. A low value implies that inertial forces predominantly drive the hydrodynamics of the flow in this setup.

# 4.2. Liquid interface

Figs. 5 and 6 show the positions of the liquid interface of the jet at different instances in time as viewed from different viewing planes. We see long ligaments, irregular droplet structures and We are able to capture complex and chaotic breakup activity comprising primary and secondary atomization that begins approximately 6 mm away from the bell edge. Primary atomization is characterized by the processes of ligament thinning, Rayleigh-Plateau instability growth and aerodynamic breakup due to interaction with quiescent air. Sinuous instabilities are observed in both cases but seem suppressed in the electrified jet. The reason for suppressed instability growth will be discussed in the following sections. As seen in Fig. 4, the electric force, which points radially outward, elongates the electrified jet along the x-direction and enhances breakup activity.

#### 4.3. Visualizing the database

The droplet ancestry statistics extraction tool operates throughout the simulation. As described in Section 3.2, the extraction tool identifies each breakup and coalescence event that occurs in the simulation and connects successive events to create an ancestry or family tree describing the breakup process. Statistics on the droplet shape, size, and location along with a characterization of the local flow field are also extracted and connected to parent and child droplets. Fig. 7 displays the ancestry as interpreted by a Neo4j graphical database. The nodes represent individual droplets and the lines connecting them represent the associated breakup events. The ligament core is in the center of the image. To maintain the visibility of the nodes and lines, only droplets which broke up up-to six times and their "ancestors" are displayed in the image. The statistics associated with each node are stored in the well organized database that can be processed to provide insights on the breakup mechanisms in ERBAs.



Fig. 5. Liquid interface positions in the non-electrified (yellow) and the electrified (violet) jet after exiting the edge of the bell on an x-y plane at different times. The nozzle is shown for reference at the top left corner and is not to scale. (For interpretation of the references to color in this figure legend, the reader is referred to the web version of this article.)

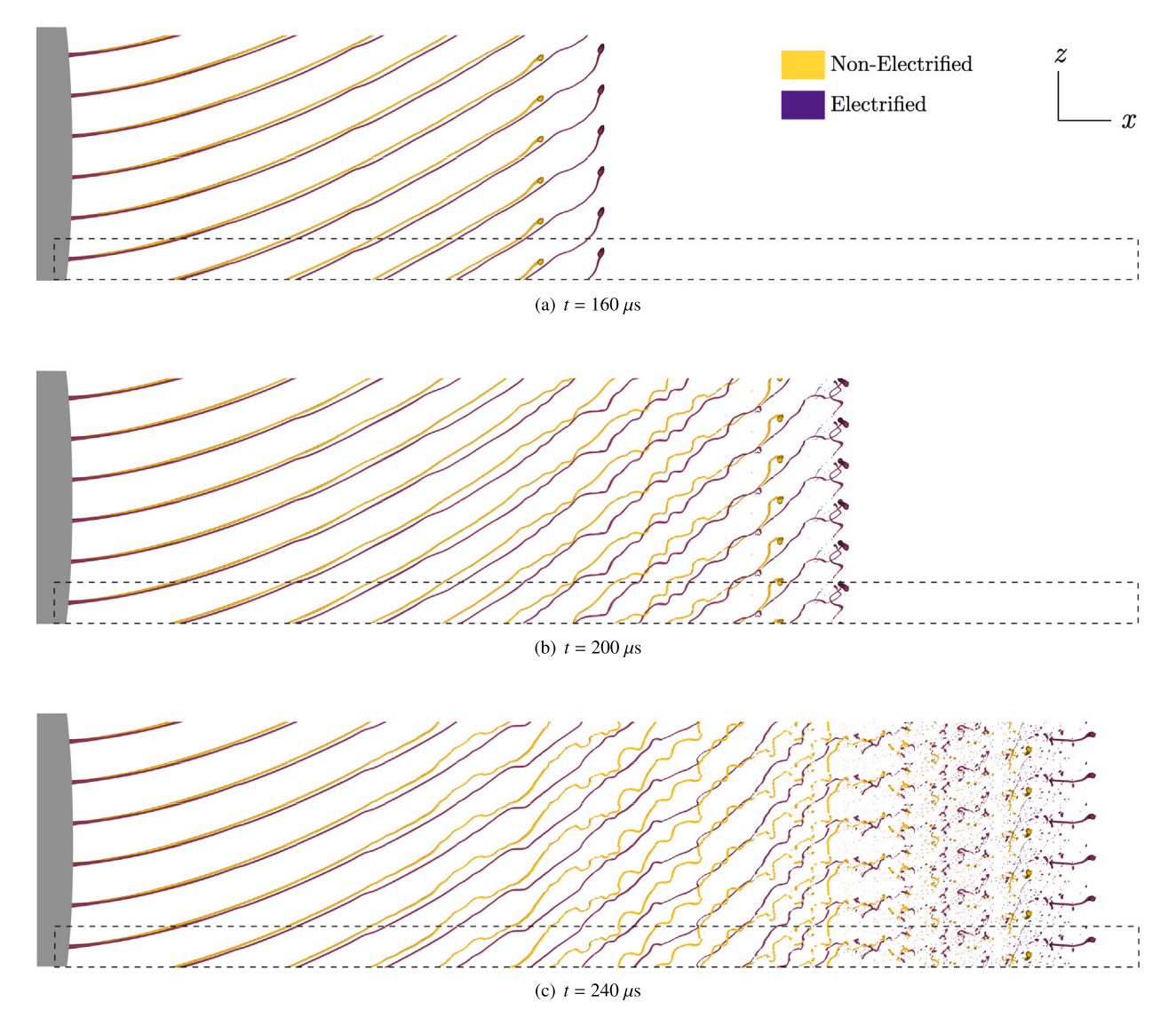


**Fig. 6.** Liquid interface positions of six individual non-electrified (yellow) and electrified (violet) jets exiting a clockwise-rotating serrated bell edge (left, not to scale) as viewed at different times from an *x-z* plane. The simulation domain is outlined by a dashed box. Owing to the periodic boundary conditions along the *z*-axis, an arc along the bell edge spanning six serrations is depicted in this view by stacking the domains in an attempt to recreate experimental images available in Shirota et al. (2012), Oswald et al. (2019), Domnick (2010) and Wilson et al. (2018). (For interpretation of the references to color in this figure legend, the reader is referred to the web version of this article.)

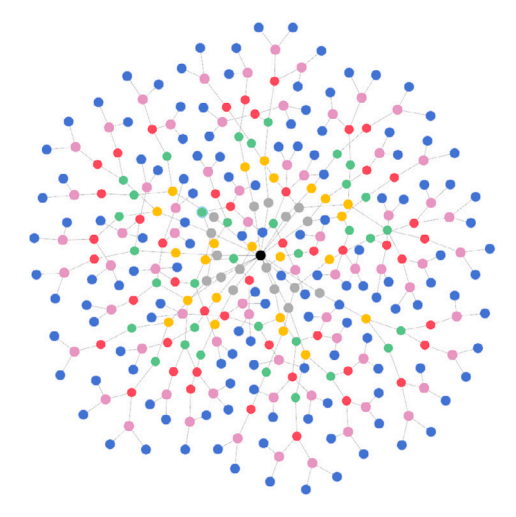


Fig. 7. Droplet ancestries in the non-electrified jet represented using the Neo4j graphical database. The colors represent breakup levels 1 (gray), 2 (yellow), 3 (green), 4 (red), 5 (pink) and 6 (blue). Lines connect related droplets, i.e., droplets which split from each other. The ligament core (black) is present at the center of the image. Each node contains relevant statistics from the breakup event. (For interpretation of the references to color in this figure legend, the reader is referred to the web version of this article.)

#### 4.4. Spray characteristics

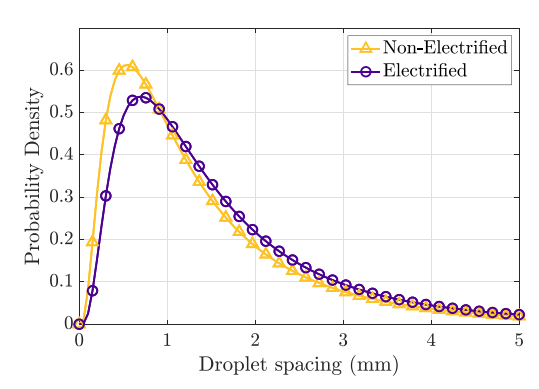
The spray statistics point to the observation that electrification enhances breakup activity. The radial liquid penetration after 300 µs is 5% more for the electrified jet. The spray angle characterizes the dispersion of the spray and is computed as the angle about the z axis on the x-y plane out of the bell edge such that 90% of the liquid is within the prescribed region created by that angle. The spray angle is about 3.4 times greater for the electrified jet. The distribution of droplet spacing (Fig. 8(a)), which can be quantified as the distance between every droplet pair in the spray, further reflects the larger spray coverage in the electrified jet where the mean droplet spacing which is 12% more than the non-electrified case. These metrics suggest that atomization and breakup activity is mildly enhanced by the electric field. As seen in Fig. 4, the electric force points radially outward and increases penetration and spray coverage in electrified flows. Droplet spacing is an important metric in rotary sprays and the electric field has a significant impact on it. The optimal operating conditions of the electrified atomizer have to be carefully selected.

In contrast, the breakup length, i.e., the length of the main ligament core, is 4% longer for the electrified jet. Moreover, the first instance of breakup occurs 6% later in the electrified jet. This can be attributed to the stabilizing force provided by the electric field on the charged liquid core (Bhuptani and Sathian, 2017; Saville, 1971; Nayyar and Murty, 1960; Saville, 1970; Mestel, 1996).

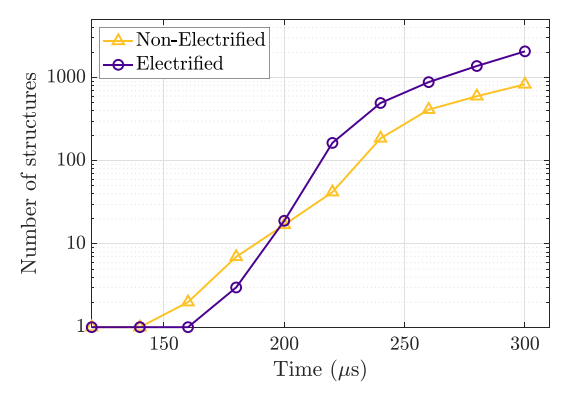
These numbers suggest that although there is an evident trend, the impact of the electric field on the atomizing spray characteristics is minor. This effect, albeit minimal, is persistent in time. However, in the next section, we explain that once breakup begins, the electric field accelerates the breakup process leading to secondary atomization.

#### 4.5. Atomization characteristics

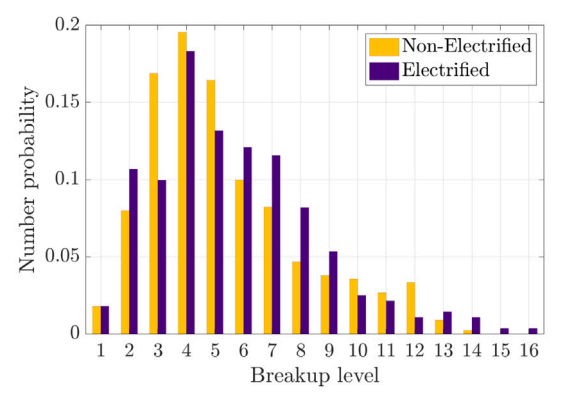
According to Pendar and Páscoa (2021), the presence of electric charges within liquid structures causes a net reduction in the effective surface tension in large droplets and ligaments and therefore an increase in their effective local Weber number. This leads to enhanced breakup activity. After 300  $\mu$ s, the electrified jet contains about 25% more droplets than the non-electrified jet. Fig. 8(b) shows the time evolution of the number of liquid structures in the domain. The delay



(a) Log-normal fit of the near-bell droplet spacing probabilty density.



(b) The total number of droplets in the domain over time. Note the logarithmic scale on the *y*-axis.

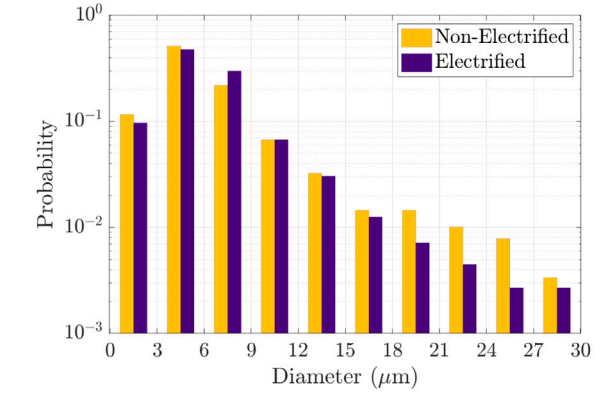


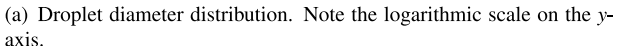
(c) The number distribution of droplets that have undergone different breakups levels.

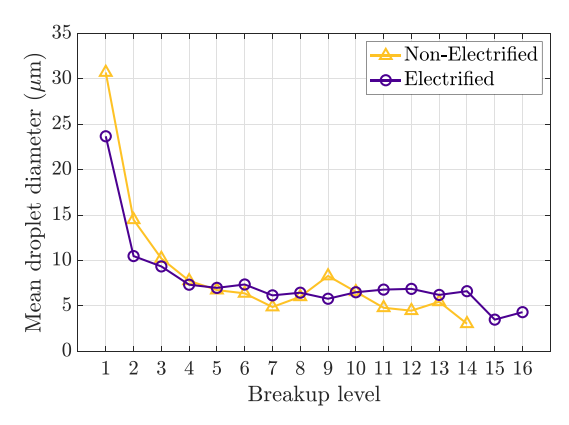
Fig. 8. Comparing atomization characteristics in non-electrified (yellow) and electrified (violet) operating conditions in the first 300  $\mu$ s of the near-bell atomization simulation. (For interpretation of the references to color in this figure legend, the reader is referred to the web version of this article.)

in the first instance of breakup (discussed in the previous section) and the accelerated breakup in the electrified jet are evident from the plot. A closer look at the droplet statistics, which will be presented in the following sections, provides more evidence for the enhanced atomization in an electrified jet.

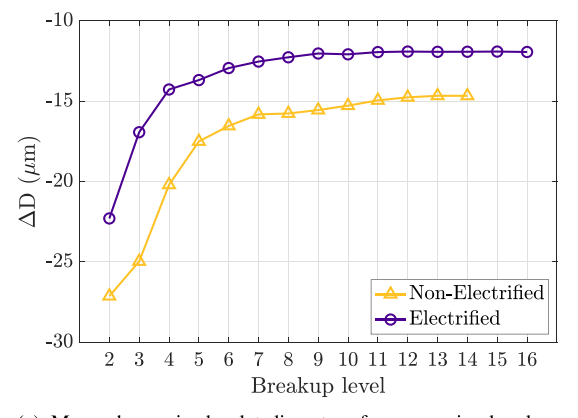
We identify the two major types of atomization in this system — primary and secondary (Saye et al., 2023). Primary atomization occurs when droplets split from the main ligament core. Secondary atomization comprises all breakup following primary atomization which includes second, third, fourth, etc. breakup events. These subsequent



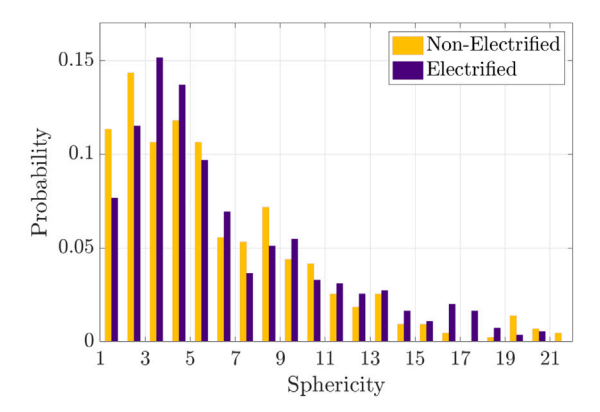




(b) Mean droplet diameter for each breakup level.



(c) Mean change in droplet diameters for successive breakup levels. Here, breakup level 1 is omitted since it corresponds to breakup from the main ligament core.



(d) Droplet sphericity distribution.

Fig. 9. Comparing size and shape related droplet statistics in non-electrified (yellow) and electrified (violet) operating conditions during the first 300  $\mu$ s of the near-bell atomization simulation. (For interpretation of the references to color in this figure legend, the reader is referred to the web version of this article.)

breakup events are also called breakup levels in the following discussion. For clarity, breakup level 1 corresponds to liquid structures that are formed due to primary atomization, i.e., breakup from the main ligament core; breakup levels 2 onward correspond to liquid structures created from secondary atomization events. The statistics listed in this paragraph are computed by comparing a total of 1119 droplets produced in the electrified jet to 837 produced in the nonelectrified jet. In the non-electrified jet, 1.64% of the total number of droplets formed in the simulation are from primary atomization (broke up once) and 98.36% are from secondary atomization (broke up two or more times). The prevalence of secondary atomizing events indicates that the droplet cloud is heavily dependent on mechanisms within this regime. The dominance is more pronounced when examining the number of secondary breakup events in the electrified jet (3310) which is 53% more than that in the non-electrified jet (2161). Moreover, the ratio of secondary to primary droplets in the electrified jet (80.73) is 34.5% more than that in the non-electrified jet (60.02). This follows the idea that the electric field accelerates secondary breakup activity. Various parameters including the rotation rate, surface tension coefficient, and liquid viscosity affect the distance and time at which primary atomization begins.

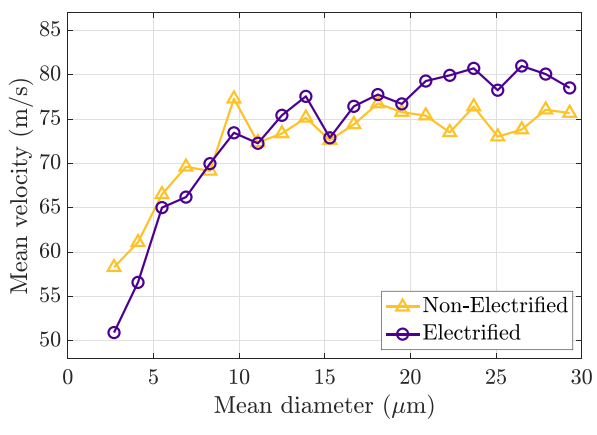
It is interesting to analyze the number of droplets for each breakup level. While the final time chosen is arbitrary, it confirms the trend of atomization activity in the domain. Fig. 8(c) shows the number distribution of the droplets for each breakup level in the simulation. Although the dominant breakup level for both cases is the same (level 4), the electrified jet, which contains more droplets overall, also contains more droplets in deeper breakup levels.

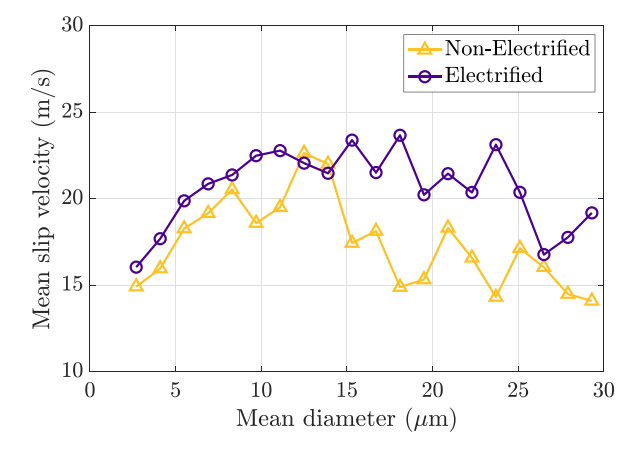
Droplet coalescence is a crucial process in atomizing flows. After 300  $\mu s$ , the ratio of coalescence to breakup events in electrified operation (0.27) is 41% more than that in the non-electrified setup (0.19). It makes intuitive sense that more coalescence is observed in electrified setups because although the droplets are more spread out, the spray cloud contains more structures which in turn leads to more droplet collisions.

# 4.6. Droplet size and shape evolution

The enhanced breakup activity in the electrified jet produces smaller droplets. The mean diameter of droplets in the spray cloud near the nozzle is about 4.5% smaller when operating in an electric field. Fig. 9(a) shows a comparison of the diameter distribution of droplets in the domain. We observe that more number of smaller liquid structures are created in an electrified jet due to the net reduction in effective surface tension in charged droplets. Fig. 9(b) shows the comparison of the mean droplet diameters for each breakup level. A trend towards decreasing droplet sizes for deeper breakup levels is generally observed. Due to coalescence events, the droplet sizes may not strictly decrease between successive breakup levels.

Fig. 9(c) shows the mean change in diameter of droplets between successive breakup levels. The change in the size of droplets decreases for deeper breakup levels due to the small sizes of the droplets themselves. The mean change in diameters across all breakup levels is about 18% lower in electrified jets. There are some instances where the change in diameter during a breakup event, which is the difference





- (a) Comparing the mean velocity for different droplet sizes.
- (b) Comparing the mean slip velocity for different droplet sizes.

Fig. 10. Comparing velocity characteristics related to droplet size for near-bell atomization in non-electrified (yellow) and electrified (violet) operating conditions during the first 300 μs of the near-bell atomization simulation.

between the new and parent droplet diameters, is greater than zero, implying that the child droplet is larger than the parent. This is due to a coalescence event that occurred between two breakup events leading to an increase in its size. After breakup level 9, the mean change in diameter across breakup levels is seemingly constant for both cases. This is speculated to be due to a high ratio of coalescence to breakup events in this regime.

One way to quantify the shape of the resulting droplet is to examine its sphericity — a dimensionless quantity that represents the degree of departure from a perfect sphere. Mathematically, sphericity can be calculated as  $A_1/A_3$ , where  $A_1 \geq A_2 \geq A_3$  are the lengths of the three principal axes of an ellipsoidal approximation of the droplet structure. A sphericity of 1, which is its lowest attainable value, indicates a perfect sphere, while larger values indicate irregular shapes. Fig. 9(d) shows a comparison of the sphericity distribution of droplets in the domain. The mean sphericity of all droplet structures is about 5% lower for the electrified droplets after 300  $\mu s$  of the simulation, suggesting that they are more spherical in shape.

#### 4.7. Droplet velocity statistics

Analyzing the droplet velocities shows that during breakup, the mean absolute velocity of droplets in the electrified jet is about 3% lower than the non-electrified jet during breakup events. Fig. 10(a) shows that smaller droplets undergo breakup at lower velocities in the electrified jet due to the net reduction in the effective surface tension force. However, larger droplets undergo breakup at greater velocities in the electrified jet. This can be attributed to the presence of charges which imparts electric force on large droplets. A similar trend is not evident in smaller droplets due to their small size and sensitivity to aerodynamic drag. Additionally, the mean slip velocity magnitude, which is formulated as  $|U_{\rm liquid}-U_{\rm gas}|$  , is 16% higher in an electrified setup during breakup events. This suggests that charged droplets undergo breakup at higher slip velocities. Fig. 10(b) highlights that this is true across most droplets sizes.  $|U_{\text{liquid}}|$  is computed as the liquid volume weighted average velocity of cells corresponding to that structure while  $|U_{\rm gas}|$  is computed as the gas volume weighted average velocity of cells neighboring the interfacial cells of that structure. It is important to note here that this method of calculating the slip velocity is a severe underestimation. While its actual value is challenging to compute, our observation that its magnitude is higher in an electrified jet is a useful statistic which will be discussed in the next section.

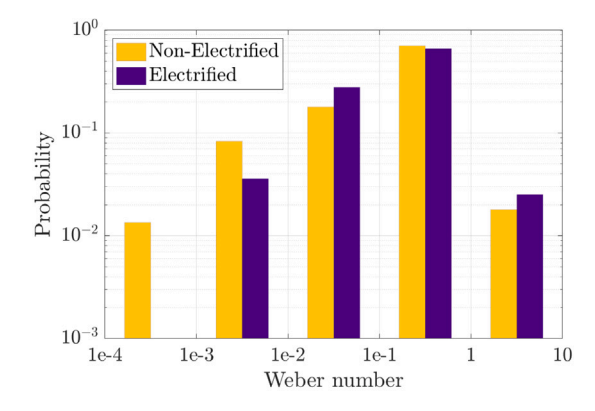


**Fig. 11.** Local Weber number distribution associated with all structures. Note the logarithmic scale on the *y*-axis. (For interpretation of the references to color in this figure legend, the reader is referred to the web version of this article.)

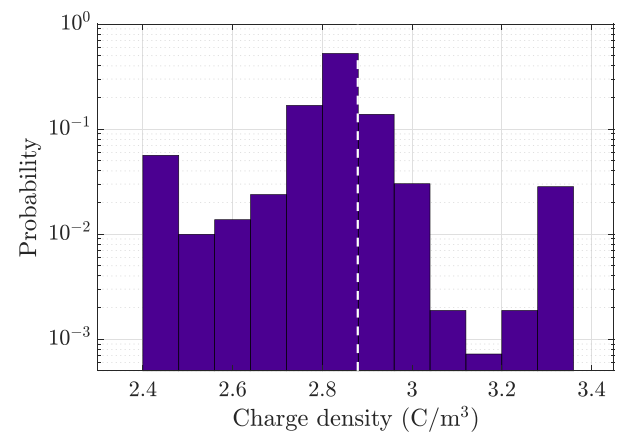
#### 4.8. Local Weber number analysis

Using the ancestry extraction tool, the local flow field surrounding breakup events is analyzed and the local Weber number (We  $_{\rm local}$ ) is computed as

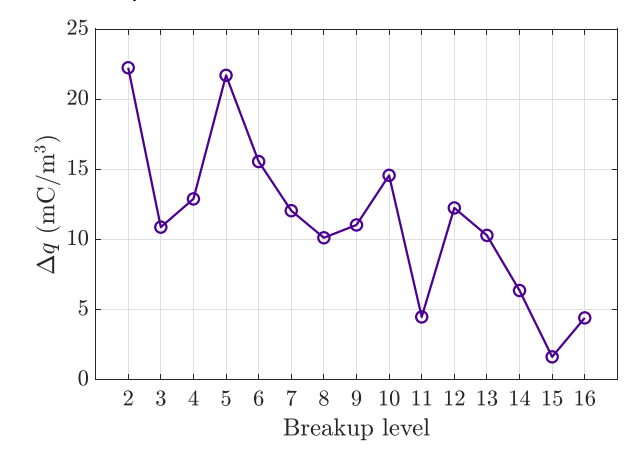
We 
$$_{local} = \frac{\rho_g U_s^2 L}{\gamma}$$
 (17)

where  $\rho_g$  is the gas density,  $U_s$  is the slip velocity, L is the characteristic length which is the equivalent spherical diameter of the droplet prior to breakup, and  $\gamma$  is the surface tension coefficient. A more detailed explanation of this calculation is provided in Christensen and Owkes (2023).

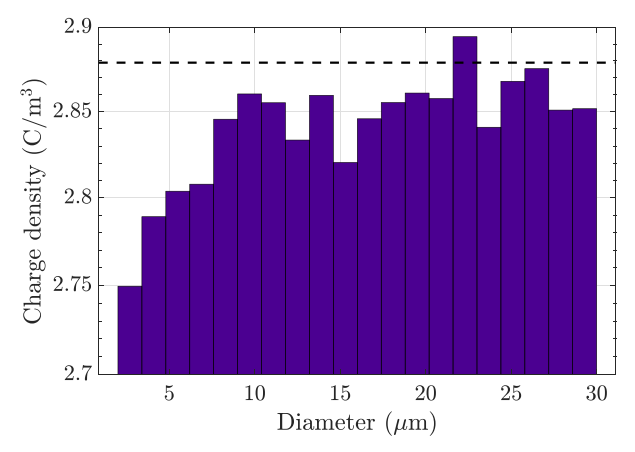
The We  $_{\rm local}$  distribution corresponding to structures prior to breakup is presented in Fig. 11. The mean Weber number for all breakup events is about 25% more in an electrified jet, which likely indicates that aerodynamic forces are more actively driving atomization in this system. This follows the findings of the slip velocity which was higher during breakup in electrified droplets. To reiterate, the slip velocity, which is severely underestimated, is squared in Eq. (17) to calculate the We  $_{\rm local}$ . While the accurate value of We  $_{\rm local}$  is challenging to compute, the general trend that it is higher in electrified setups is a useful finding. Since the We  $_{\rm local}$  is severely underestimated in this formulation, we have sufficient reason to believe that atomization is driven by both aerodynamic breakup and instability growth and is enhanced in electrified setups by the electric force and the presence of charges in the liquid.



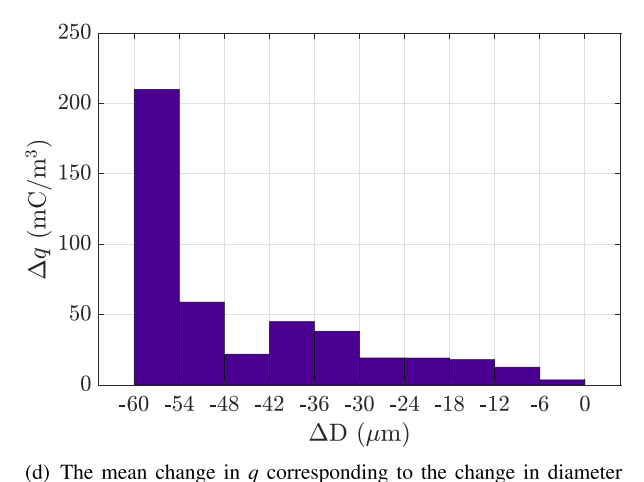
(a) Number distribution of q in liquid structres in the domain. The inital bulk value of q is shown as a dashed line. Note the logarithmic scale on the y-axis.



(c) The mean change in  $\boldsymbol{q}$  between successive breakup levels.



(b) Mean q in liquid structures of different sizes. The inital bulk value of q is shown as a dashed line.



(d) The mean change in q corresponding to the change in diameter during a breakup event.

Fig. 12. Comparing charge density characteristics for near-bell atomization in electrified operation during the first 300 µs of the near-bell atomization simulation.

# 4.9. Charge distribution statistics

Most droplets contain a charge density that is very close to the initial bulk charging value (Fig. 12(a)). However, since the process of charge migration is included in the model, we also see a distribution of charge densities in the droplets. Compared to the initial charge density (Table 1), it is more probable to find a droplet with a lower value of a. As charges relax towards the interface of the ligament, there is a localized reduction of q in the bulk of the ligament. A majority of the liquid structures break off the ligament bulk (since a greater liquid volume is present in the bulk than near the interface) to form droplets that contain slightly lower values of q than the initial bulk value. The moderate value of Re<sub>e</sub> (Table 2) which is the ratio of the residence time of liquid in the domain to the charge relaxation timescale indicates that the charges have time to relax to some degree, but not enough time to fully relax to the surface. Higher resolution simulations can help better understand the charge relaxation process through the ligament core and the factors affecting the charge distribution in the spray cloud.

Upon closer inspection of the charge distribution in droplets, we see that q is generally higher in larger droplets (Fig. 12(b)). This can be explained as follows — small droplets are more likely to be formed from the volume of liquid in the bulk of a ligament which, as discussed, contains a lower charge density. Larger droplets tend to break off as long primary ligaments from the main ligament core and therefore will not necessarily have a lower value of q.

The change in q for successive breakup levels also shows a decreasing trend and approaches zero for the deepest breakup levels

(Fig. 12(c)). Naturally, the change in q during a breakup event is inversely proportional to the change in the droplet sizes (Fig. 12(d)).

# 5. Conclusions

Electrostatic rotary bell atomizers (ERBAs) are popular atomizing devices used in various industries, including automotive painting. Multiple complex physical processes influence the mechanisms driving atomization in the device. In this work, we perform high fidelity simulations using a numerical model previously developed to simulate electrohydrodynamic atomization in ERBAs. The simulations are equipped with a droplet ancestry extraction tool that stores droplet and local flow statistics. We conduct analyses on the extracted statistics to provide insights into the breakup mechanisms in an ERBA. This is a cost-effective method to understand atomization and the extract information that are challenging to obtain experimentally.

We find that the electric field has a minor impact on the atomization quality. Electrification increases jet penetration, spray angle, and droplet spacing due to the effect of the electric force that acts along the radially outward direction. However, the breakup length and the first instance of breakup in time is longer in the electrified jet due to a stabilizing force provided by the electric field on the charged ligament core. However, once breakup begins, the net reduction in the effective surface tension in liquid structures due to the presence of charges accelerates the breakup process leading enhanced secondary atomization in the electrified jet. The total number of droplets, the

ratio of secondary to primary droplets, and the ratio of coalescence to breakup activity are all higher when operating in an electric field. Charged droplets seem to undergo breakup at higher slip velocities than uncharged droplets. Most charged droplets contain a charge density that is very close to the initial bulk charging value. While larger droplets generally contain a higher value of charge density, it is more probable to find droplets with charge density values lower than the initial bulk value.

Small improvements to the performance of this device can have significant financial and environmental benefits. The findings of this work can help manufacturers choose optimal operating conditions of ERBAs more carefully. The tool developed can be employed to understand the effect of the electric field over a wide range of other operating parameters, including rotation rate, flow rate, bell potential and liquid charge density. In future work, higher-resolution simulations will be conducted to understand the charge relaxation dynamics for non-uniform initial liquid charge distributions and include the effects of a shaping air setup. The impact of the electric field on atomization will be examined for a range of parameters such as the electric Reynolds numbers and liquid Weber numbers. We hope to publish an article presenting further efforts in understanding the charge dynamics in the liquid phase in the future. Such development will allow for a deeper understanding of the electrically assisted atomization for industrial applications of ERBAs.

#### CRediT authorship contribution statement

Venkata Krisshna: Data curation, Formal analysis, Investigation, Methodology, Validation, Visualization, Writing – original draft. Mark Owkes: Conceptualization, Funding acquisition, Project administration, Resources, Software, Supervision, Writing – review & editing.

# Declaration of competing interest

The authors declare the following financial interests/personal relationships which may be considered as potential competing interests: Mark Owkes reports financial support was provided by National Science Foundation.

#### Data availability

The authors do not have permission to share data.

# Acknowledgments

This material is based upon work supported by the National Science Foundation, United States under Grant No. 1749779. The authors wish to extend their gratitude to Brendan Christensen of Montana State University for providing assistance with incorporating the droplet ancestry extraction tool to ERBA flows. The authors are grateful to PPG industries for providing valuable empirical data on the shear-thinning behavior of automotive paints. The authors are grateful to Dr. Wanjiao Liu, Dr. Kevin Ellwood and Dr. Brandon Petrouskie for many insightful discussions and advice. Computational efforts were performed on the Hyalite High Performance Computing System and the Tempest High Performance Computing System, operated and supported by University Information Technology Research Cyberinfrastructure at Montana State University. The authors would also like to extend their gratitude to Coltran Hophan-Nichols and Kenny Hanson for providing assistance with the computational resources required to seamlessly carry out the large-scale simulations in this project.

#### References

- Ahmad, A.D., Singh, B.B., Doerre, M., Abubaker, A.M., Arabghahestani, M., Salaimeh, A.A., Akafuah, N.K., 2019. Spatial positioning and operating parameters of a rotary bell sprayer: 3D mapping of droplet size distributions. Fluids 4 (3).
- Akafuah, N., Poozesh, S., Salaimeh, A., Patrick, G., Lawler, K., Saito, K., 2016. Evolution of the automotive body coating process A review. Coatings 6 (2).
- Akafuah, N.K., Toda, K., Salazar, A., Saito, K., 2013. Automotive paint spray characterization and visualization. In: Automotive Painting Technology: A Monozukuri-Hitozukuri Perspective. Springer Netherlands, Dordrecht, pp. 121–165.
- Anukiruthika, T., Moses, J., Anandharamakrishnan, C., 2021. Electrohydrodynamic drying of foods: Principle, applications, and prospects. J. Food Eng. 295, 110449.
- Azizian, P., Azarmanesh, M., Dejam, M., Mohammadi, M., Shamsi, M., Sanati-Nezhad, A., Mohamad, A.A., 2019. Electrohydrodynamic formation of single and double emulsions for low interfacial tension multiphase systems within microfluidics. Chem. Eng. Sci. 195, 201–207.
- Bailey, A.G., 1974. Electrostatic atomization of liquids. Sci. Prog. (1933- ) 61 (244), 555-581
- Balachandran, W., Bailey, A.G., 1984. The dispersion of liquids using centrifugal and electrostatic forces. IEEE Trans. Ind. Appl. IA-20 (3), 682–686.
- Berthier, J., Brakke, K.A., 2012. The Physics of Microdroplets. John Wiley & Sons.
- Bhuptani, D.K., Sathian, S.P., 2017. Effect of axial electric field on the Rayleigh instability at small length scales. Phys. Rev. E 95 (5–1), 053115.
- Blanquart, G., Pepiot-Desjardins, P., Pitsch, H., 2009. Chemical mechanism for high temperature combustion of engine relevant fuels with emphasis on soot precursors. Combust. Flame 156 (3), 588–607.
- Chen, X., Cheng, J., Yin, X., 2003. Advances and applications of electrohydrodynamics. Chin. Sci. Bull. 48 (11), 1055–1063.
- Christensen, B., Owkes, M., 2023. Efficient extraction of atomization processes from high-fidelity simulations. Comput. & Fluids 254, 105808.
- Clément, Z., Fredrik, E., Andreas, M., Oliver, H., 2014. Efficient numerical simulation of spray painting processes in automotive manufacturing. In: 23rd SAE Brasil International Congress and Display. SAE Technical Paper.
- Colbert, S.A., 2007. Numerical Simulations of Droplet Trajectories from an Electrostatic Rotary-Bell Atomizer (Ph.D. thesis). Drexel University.
- Colbert, S.A., Cairncross, R.A., 2005. A computer simulation for predicting electrostatic spray coating patterns. Powder Technol. 151, 77–86.
- Corbeels, P.L., Senser, D.W., Lefebvre, A.H., 1992. Atomization characteristics of a high speed rotary-bell paint applicator. At. Spray. 2 (2), 87–99.
- Craig, I.P., Hewitt, A., Terry, H., 2014. Rotary atomiser design requirements for optimum pesticide application efficiency. Crop Prot. 66, 34–39.
- Crowley, J.M., 1986. first ed. Fundamentals of Applied Electrostatics, vol. 1, Wiley.
- Darwish Ahmad, A., Abubaker, A.M., Salaimeh, A.A., Akafuah, N.K., 2018. Schlieren visualization of shaping air during operation of an electrostatic rotary bell sprayer: Impact of shaping air on droplet atomization and transport. Coatings 8 (8).
- Desjardins, O., Blanquart, G., Balarac, G., Pitsch, H., 2008a. High order conservative finite difference scheme for variable density low mach number turbulent flows. J. Comput. Phys. 227, 7125–7159.
- Desjardins, O., Moureau, V., Pitsch, H., 2008b. An accurate conservative level set/ghost fluid method for simulating turbulent atomization. J. Comput. Phys. 227, 8395–8416.
- Dombrowski, N., Lloyd, T., 1974. Atomisation of liquids by spinning cups. Chem. Eng. J. 8 (1), 63–81.
- Domnick, J., 2010. Effect of bell geometry in high-speed rotary bell atomization.
- Domnick, J., Scheibe, A., Ye, Q., 2005. The simulation of the electrostatic spray painting process with high-speed rotary bell atomizers. Part I: Direct charging. Part. Part. Syst. Charact. 22 (2), 141–150.
- Domnick, J., Scheibe, A., Ye, Q., 2006. The simulation of electrostatic spray painting process with high-speed rotary bell atomizers. Part II: External charging. Part. Part. Syst. Charact. 23 (5), 408–416.
- Domnick, J., Thieme, M., 2006. Atomization characteristics of high-speed rotary bell atomizers. At. Spray. 16 (8), 857–874.
- Eagles, P.A.M., Qureshi, A.N., Jayasinghe, S.N., 2006. Electrohydrodynamic jetting of mouse neuronal cells. Biochem. J. 394 (2), 375–378.
- Ellwood, K.R., Braslaw, J., 1998. A finite-element model for an electrostatic bell sprayer. J. Electrost. 45 (1), 1–23.
- Ellwood, K.R., Tardiff, J.L., Alaie, S.M., 2014. A simplified analysis method for correlating rotary atomizer performance on droplet size and coating appearance. J. Coat. Technol. Res. 11 (3), 303–309.
- Enayati, M., Chang, M.W., Bragman, F., Edirisinghe, M., Stride, E., 2011. Electrohydro-dynamic preparation of particles, capsules and bubbles for biomedical engineering applications. Colloids Surf. A 382 (1–3), 154–164.
- Farook, U., Stride, E., Edirisinghe, M.J., Moaleji, R., 2007. Microbubbling by co-axial electrohydrodynamic atomization. Med. Biol. Eng. Comput. 45 (8), 781–789.
- Fredrich, D., Weiand, E., Giusti, A., 2022. Electrostatic fields for the control of evaporating charged fuel sprays. Int. J. Multiph. Flow 104312.
- Frost, A.R., 1981. Rotary atomization in the ligament formation mode. J. Agric. Eng. Res. 26, 63–78.
- Fylladitakis, E.D., Theodoridis, M.P., Moronis, A.X., 2014. Review on the history, research, and applications of electrohydrodynamics. IEEE Trans. Plasma Sci. 42 (2), 358–375.

- Geffen, C., Rothenberg, S., 2000. Suppliers and environmental innovation: the automotive paint process. Int. J. Oper. Prod. Manage.
- Gödeke, L., Oswald, W., Willenbacher, N., Ehrhard, P., 2021. Dimensional analysis of droplet size and ligament length during high-speed rotary bell atomization. J. Coat. Technol. Res. 18, 75–81.
- Gorty, A.V., Barringer, S.A., 2011. Electrohydrodynamic spraying of chocolate. J. Food Process. Preserv. 35 (4), 542–549.
- Grace, J., Marijnissen, J., 1994. A review of liquid atomization by electrical means. J. Aerosol Sci. 25 (6), 1005–1019.
- Guettler, N., Knee, P., Ye, Q., Tiedje, O., 2020. Initial droplet conditions in numerical spray painting by electrostatic rotary bell sprayers: A framework for optimization of injection model coefficients. J. Coat. Technol. Res. 17 (5), 1091–1104.
- Hayati, I., Bailey, A.I., Tadros, T.F., 1986. Mechanism of stable jet formation in electrohydrodynamic atomization. Nature 319 (6048), 41–43.
- Heindel, T.T., 2018. X-ray imaging techniques to quantify spray characteristics in the near field. At. Spray. 28 (11).
- Hendrickson, K., Weymouth, G.D., Yue, D.K.-P., 2020. Informed component label algorithm for robust identification of connected components with volume-of-fluid method. Comput. & Fluids 197, 104373.
- Hines, R.L., 1966. Electrostatic atomization and spray painting. J. Appl. Phys. 37, 2730–2736.
- Hinze, J.O., Milborn, H., 1950. Atomization of liquids by means of a rotating cup. J. Appl. Mech. 17 (2), 145–153.
- Honkanen, M., Elcock, D., Kuo, C.J., Peles, Y., Amitay, M., 2011. Lagrangian tracking of bubbles interacting with pin-fins in a microchannel. Exp. Fluids 50 (6), 1527–1538.
- Hoshen, J., Kopelman, R., 1976. Percolation and cluster distribution. I. Cluster multiple labeling technique and critical concentration algorithm. Phys. Rev. B 14 (8), 3438.
- Im, K.S., Lai, M.C., Liu, Y., Sankagiri, N., Loch, T., Nivi, H., 2000. Visualization and measurement of automotive electrostatic rotary-bell paint spray transfer processes. J. Fluids Eng. 123 (2), 237–245.
- Im\*, K.S., Lai, M.C., Yoon, S.J., 2003. Spray characteristics on the electrostatic rotating bell applicator. KSME Int. J. 17, 2053–2065.
- Im, K.S., Lai, M.C., Yu, S.T.J., Matheson, Jr., R.R., 2004. Simulation of spray transfer processes in electrostatic rotary bell sprayer. J. Fluids Eng. 126 (3), 449–456.
- Jaworek, A., Sobczyk, A., Krupa, A., 2018. Electrospray application to powder production and surface coating. J. Aerosol Sci. 125, 57–92.
- Kelly, A., 1984. The electrostatic atomization of hydrocarbons. J. Inst. Energy; (United Kingdom) 57 (431).
- Keshavarz, B., Houze, E.C., Moore, J.R., Koerner, M.R., McKinley, G.H., 2020. Rotary atomization of newtonian and viscoelastic liquids. Phys. Rev. Fluids 5 (3).
- Khan, M.K.I., Schutyser, M.A., Schroën, K., Boom, R., 2012. The potential of electrospraying for hydrophobic film coating on foods. J. Food Eng. 108, 410–416.
- Kim, K., Turnbull, R.J., 1976. Generation of charged drops of insulating liquids by electrostatic spraying. J. Appl. Phys. 47 (5), 1964–1969.
- Kourmatzis, A., Shrimpton, J.S., 2009. Electrohydrodynamics and charge injection atomizers: A review of the governing equations and turbulence. At. Spray. 19 (11), 1045–1063
- Krisshna, V., Owkes, M., 2023. High-fidelity simulations of a rotary bell atomizer with electrohydrodynamic effects. http://dx.doi.org/10.2139/ssrn.4396571, Available at SSRN: https://ssrn.com/abstract=4396571.
- Li, Z., Zhao, W., Wu, Z., 2021. Understanding transient internal flow processes in high-pressure nozzles using synchrotron radiation X-ray phase contrast imaging technology. At. Spray. 31 (4).
- Linne, M.A., Paciaroni, M., Gord, J.R., Meyer, T.R., 2005. Ballistic imaging of the liquid core for a steady jet in crossflow. Appl. Opt. 44 (31), 6627–6634.
- Loch, T., Nivi, H., Liu, Y., Lai, M.C., Im, K.S., 1998. An experimental investigation of spray transfer processes in an electrostatic rotating bell applicator. In: International Body Engineering Conference & Exposition. SAE International.
- Mackaplow, M.B., Zarraga, I.E., Morris, J.F., 2006. Rotary spray congealing of a suspension: Effect of disk speed and dispersed particle properties. J. Microencapsul. 23 (7), 793–809.
- Mahmoud, A., Youssef, M.S., 2014. Influence of spinning cup and disk atomizer configurations on droplet size and velocity characteristics. Chem. Eng. Sci. 107, 149–157.
- Mark, A., Andersson, B., Tafuri, S., Engstrom, K., Sorod, H., Edelvik, F., Carlson, J.S., 2013. Simulation of electrostatic rotary bell spray painting in automotive paint shops. At. Spray. 23 (1), 25–45.
- Melcher, J.R., 1981. Continuum Electromechanics, vol. 2, MIT press Cambridge, MA. Melcher, J.R., Taylor, G.I., 1969. Electrohydrodynamics: A review of the role of interfacial shear stresses. Annu. Rev. Fluid Mech. 1 (1), 111–146.
- Mestel, A.J., 1996. Electrohydrodynamic stability of a highly viscous jet. J. Fluid Mech. 312, 311–326.
- Naoki, I., Takuro, I., Yu, N., Seiichiro, I., Yu, F., 2019. Numerical simulation of
- droplet-formation in rotary atomizer. Theor. Appl. Mech. Lett. 9, 202–205.Nayyar, N.K., Murty, G.S., 1960. The stability of a dielectric liquid jet in the presence of a longitudinal electric field. Proc. Phys. Soc. 75 (3), 369–373.
- Ogasawara, S., Daikoku, M., Shirota, M., Inamura, T., Saito, Y., Yasumura, K., Shoji, M., Aoki, H., Miura, T., 2010. Liquid atomization using a rotary bell cup atomizer. J. Fluid Sci. Technol. 5, 464–474.

- Oswald, W., Lauk, J., Gödeke, L., Ehrhard, P., Willenbacher, N., 2019. Analysis of paint flow pulsations during high-speed rotary bell atomization. Coatings 9 (10), 1–9.
- Owkes, M., Cauble, E., Senecal, J., Currie, R.A., 2018. Importance of curvature evaluation scale for predictive simulations of dynamic gas-liquid interfaces. J. Comput. Phys. 365, 37–55.
- Owkes, M., Desjardins, O., 2014. A computational framework for conservative, threedimensional, unsplit, geometric transport with application to the volume-of-fluid (VOF) method. J. Comput. Phys. 270, 587–612.
- Owkes, M., Desjardins, O., 2015a. Consistent and conservative framework for incompressible multiphase flow simulations. In: APS Division of Fluid Dynamics Meeting Abstracts. pp. H7–007.
- Owkes, M., Desjardins, O., 2015b. A mesh-decoupled height function method for computing interface curvature. J. Comput. Phys. 281, 285–300.
- Owkes, M., Desjardins, O., 2017. A mass and momentum conserving unsplit semi-Lagrangian framework for simulating multiphase flows. J. Comput. Phys. 332, 21–46.
- Oxley, J., 2012. Spray cooling and spray chilling for food ingredient and nutraceutical encapsulation. In: Encapsulation Technologies and Delivery Systems for Food Ingredients and Nutraceuticals. Elsevier, pp. 110–130.
- Pendar, M.R., Páscoa, J.C., 2019. Numerical modeling of electrostatic spray painting transfer processes in rotary bell cup for automotive painting. Int. J. Heat Fluid Flow 80, 108499.
- Pendar, M.R., Páscoa, J.C., 2020. Atomization and spray characteristics around an ERBS using various operational models and conditions: numerical investigation. Int. J. Heat Mass Transfer 161.
- Pendar, M.R., Páscoa, J.C., 2021. Numerical analysis of charged droplets size distribution in the electrostatic coating process: Effect of different operational conditions. Phys. Fluids 33 (3), 033317.
- Precedence Research, 2019. Automotive Paints & Coatings Market Growth, Report 2020–2027 Automotive. Technical Report, Precedence Research.
- Raje, P., Murmu, N.C., 2014. A review on electrohydrodynamic-inkjet printing technology.
- Ray, R., Henshaw, P., 2018. Evaporation of clearcoat solvents from a rotary bell atomizer and its relationship with bell speed, flow rate, and electrostatic potential. J. Coat. Technol. Res. 15, 41–49.
- Rezayat, S., Farshchi, M., 2019. Spray formation by a rotary atomizer operating in the coriolis-induced stream-mode injection. At. Spray. 29 (10), 937–963.
- Rodriguez-Rodriguez, J., Gordillo, J.M., Martinez-Bazan, C., 2006. Breakup time and morphology of drops and bubbles in a high-Reynolds-number flow. J. Fluid Mech. 548, 69–86. http://dx.doi.org/10.1017/S002211200500741X.
- Rodríguez-Rodríguez, J., Martínez-Bazán, C., Montañés, J.L., 2003. A novel particle tracking and break-up detection algorithm: application to the turbulent break-up of bubbles. Meas. Sci. Technol. 14 (8), 1328.
- Rubel, C., Owkes, M., 2019. Extraction of droplet genealogies from high-fidelity atomization simulations. At. Spray. 29 (8), 709–739.
- Sadegh, P., Nelson, A., Kozo, S., 2018. Effects of automotive paint spray technology on the paint transfer efficiency – a review. Proc. Inst. Mech. Eng. D 232 (2), 282–301.
- Saville, D.A., 1970. Electrohydrodynamic stability: Fluid cylinders in longitudinal electric fields. Phys. Fluids 13 (12), 2987–2994.
- Saville, D.A., 1971. Stability of electrically charged viscous cylinders. Phys. Fluids 14 (6), 1095–1099.
- Saville, D.A., 1997. Electrohydrodynamics: The Taylor-Melcher leaky dielectric model. Annu. Rev. Fluid Mech. 29 (1), 27–64.
- Saye, R.I., Sethian, J.A., Petrouskie, B., Zatorsky, A., Lu, X., Rock, R., 2023. Insights from high-fidelity modeling of industrial rotary bell atomization. Proc. Natl. Acad. Sci. 120 (4), e2216709120.
- Sedarsky, D., Berrocal, E., Linne, M., 2010. Numerical analysis of ballistic imaging for revealing liquid breakup in dense sprays. At. Spray. 20 (5).
- Sheehy, P., Owkes, M., 2017. Numerical study of electric Reynolds number on electrohydrodynamic assisted atomization. At. Spray. 27 (7), 645–664.
- Shen, B., Ye, Q., Guettler, N., Tiedje, O., Domnick, J., 2019. Primary breakup of a non-Newtonian liquid using a high-speed rotary bell atomizer for spray-painting processes. J. Coat. Technol. Res. 16, 1581–1596.
- Shirota, M., Hatayama, Y., Haneda, T., Inamura, T., Daikoku, M., Saito, Y., Aoki, H., 2012. Formation and breakup of ligaments from a rotary bell cup atomizer.
- Shrimpton, J.S., Laoonual, Y., 2006. Dynamics of electrically charged transient evaporating sprays. Internat. J. Numer. Methods Engrg. 67 (8), 1063–1081.
- Sidawi, K., Moroz, P., Chandra, S., 2021a. Bell-cup serrations and their effect on atomization in electrostatic rotating bell atomizers. Exp. Fluids 62 (8), 1–16.
- Sidawi, K., Moroz, P., Chandra, S., 2021b. On surface area coverage by an electrostatic rotating bell atomizer. J. Coat. Technol. Res. 18, 649–663.
- Slangen, P.R., Lauret, P., Heymes, F., Aprin, L., Lecysyn, N., 2016. High-speed imaging optical techniques for shockwave and droplets atomization analysis. Opt. Eng. 55 (12), 121706.
- Stevenin, C., Bereaux, Y., Charmeau, J.Y., Balcaen, J., 2015. Shaping air flow characteristics of a high-speed rotary-bell sprayer for automotive painting processes. J. Fluids Eng. Trans. ASME 137 (11), 1–8.
- Stimpson, B.P., Evans, Jr., C.A., 1978. Electrohydrodynamic ionization mass spectrometry of biochemical materials. Biomed. Mass Spectrom. 5 (1), 52–63.

- Stuetzer, O.M., 1962. Magnetohydrodynamics and electrohydrodynamics. Phys. Fluids 5 (5), 534–544.
- Taylor, G., 1966. Studies in electrohydrodynamics. I. The circulation produced in a drop by electrical field. Proc. R. Soc. A 291 (1425), 159–166.
- Turnbull, R., 1989. Self-acceleration of a charged jet. IEEE Trans. Ind. Appl. 25 (4), 699-704.
- Van Poppel, B., Desjardins, O., Daily, J.W., 2010. A ghost fluid, level set methodology for simulating multiphase electrohydrodynamic flows with application to liquid fuel injection. J. Comput. Phys. 229, 7977–7996.
- Viti, V., Kulkarni, J., Watve, A., 2010. Computational fluid dynamics analysis of the electrostatic spray painting process with a rotating bell cup. At. Spray. 20 (1), 1–17.
- Wang, Y., Im, K.S., Fezzaa, K., Lee, W., Wang, J., Micheli, P., Laub, C., 2006. Quantitative x-ray phase-contrast imaging of air-assisted water sprays with high Weber numbers. Appl. Phys. Lett. 89 (15), 151913.
- Wang, X.T., Ning, Z., Lü, M., 2019. Linear instability of a charged non-Newtonian liquid jet under an axial electric field. J. Appl. Phys. 126 (13), 135301.
- Wilson, J.E., Grib, S.W., Darwish Ahmad, A., Renfro, M.W., Adams, S.A., Salaimeh, A.A., 2018. Study of near-cup droplet breakup of an automotive electrostatic rotary bell (ESRB) atomizer using high-speed shadowgraph imaging. Coatings 8 (5).
- Yamamoto, T., Velkoff, H., 1981. Electrohydrodynamics in an electrostatic precipitator. J. Fluid Mech. 108, 1–18.